Dynamics of an antiferromagnetic skyrmion in a racetrack with a defect

Xue Liang,[1] Guoping Zhao,[1,*] Laichuan Shen,[2] Jing Xia,[2] Li Zhao,[1] Xichao Zhang,[2] and Yan Zhou[2,†]
[1]*College of Physics and Electronic Engineering, Sichuan Normal University, Chengdu 610068, China*
[2]*School of Science and Engineering, The Chinese University of Hong Kong, Shenzhen, Guangdong 518172, China*

(Received 18 March 2019; revised manuscript received 28 August 2019; published 28 October 2019)

The antiferromagnetic skyrmion is a promising building block for future antiferromagnetic spintronic devices, which has several advantages, including ultrafast dynamics and zero skyrmion Hall angle. The understanding of the pinning and depinning of an antiferromagnetic skyrmion to defects is a prerequisite for skyrmion-based in-line motion applications, such as racetrack memory. Here, we numerically study the effect of two types of defects caused by the local decrease/increase of perpendicular magnetic anisotropy on the current-induced dynamics of an antiferromagnetic skyrmion, where the critical depinning current density of the skyrmion motion for different defects is determined under the framework of micromagnetics. We also provide an explanation for the complex behaviors of the antiferromagnetic skyrmion via energy landscape, which shows that the skyrmion always prefers to stay at a specific place with minimal energy. Furthermore, the current-induced motion of a skyrmion in an antiferromagnetic racetrack with defects is compared to that in a ferromagnetic racetrack. Our results are useful for the understanding of antiferromagnetic skyrmion physics at low temperatures and could provide guidelines for designing applications based on antiferromagnetic skyrmions.

DOI: 10.1103/PhysRevB.100.144439

I. INTRODUCTION

Magnetic skyrmions are topologically nontrivial and particlelike swirling spin configurations, which have aroused a lot of interest from the viewpoints of their attractive physics [1,2] and potential applications in spintronic devices [3–8].

They were first observed in noncentrosymmetric magnets, such as MnSi [9–11], $Fe_{1-x}Co_xSi$ [12–13], FeGe [14], and $Mn_{1-x}Fe_xGe$ [15]. Due to their small size, topological structure, and low critical depinning current density [2,5,11,16–21], skyrmions could be employed as information carriers in future nanoscale magnetic data storage [22] and logic devices [6] with ultrahigh density and low-energy consumption. Recently, much interest has also been devoted to the skyrmion in antiferromagnetic (AFM) materials [23–36]. In AFM system, the neighboring magnetic moments are arranged in antiparallel by the AFM exchange coupling interaction between sublattices, resulting in zero magnetization at the macroscopic scale [37–41]. Consequently, perfect AFM materials are insensitive to external disturbance and have no magnetic stray field, thus improving the robustness against magnetic perturbations.

Compared with the skyrmions in ferromagnetic (FM) materials, those in AFM materials hold two prominent merits. First, AFM skyrmions show no skyrmion Hall effect so that they can go straightly to the direction we expected [23–25,28–30,32,34]. For example, considering an applied current, AFM skyrmions can move in straight lines along the driving current direction [28–30]. Second, AFM skyrmions move faster under the same external driving force, and their speed can reach several kilometers per second without the annihilation of skyrmions [24,29]. In addition, the AFM materials are more abundant in nature, which include metals comprised Mn-based alloys, insulators, semiconductors and semimetals [28,31,41–43]. These attractive features of AFM skyrmions have led to the recent rapid development of AFM spintronics, which open a novel path to the concepts of magnetic memories based on skyrmions and domain walls which are potentially expected to replace the traditional FM counterparts.

To design the future spintronic device applications based on AFM skyrmions, it is necessary and important to study the creation, transmission and detection of skyrmions in AFM materials [23,24,28–36]. Particularly, extensive theoretical works have already been performed on the dynamics of AFM skyrmions based on the ideal systems. However, there are inevitable defects and impurities in actual materials, which may have a nonnegligible effect on the motion of skyrmions. For example, in FM system, the skyrmion may be deflected, distorted, and even captured by imperfections, which are caused by the local maxima in magnetic exchange [44,45], inhomogeneous magnetic anisotropy [17,46,47], single atomic defect [48,49], or vacancies in magnetic films [50]. It is obvious that the material defects play a vital role in the dynamics of FM skyrmions; however, the effect of material defects on AFM skyrmion dynamics remains elusive. Silva *et al.* [51] have investigated how hole defects influence the current-induced motion of AFM skyrmions in a racetrack, and found that the AFM skyrmion can be captured, scattered or completely destroyed by a hole. Here, we aim to consider an AFM film with a defect induced by the local variation in the perpendicular magnetic anisotropy (PMA), and discuss the dynamic pinning and depinning processes of an AFM skyrmion. Our results show that the AFM skyrmion

*zhaogp@uestc.edu.cn
†zhouyan@cuhk.edu.cn

spontaneously moves to a specific location (position of the energy minimum) when it is placed in the vicinity of the defect, and the defect acts as an obstacle that can result in an effective slowdown or even capturing of the AFM skyrmion during its motion, which depends on the parameters of defect and driving current density.

The remaining of this paper is organized as follows. In Sec. II we provide a brief description of our theoretical framework and calculation model. Sec. III contains our numerical results: the dynamic pinning and depinning processes of the AFM skyrmion in the presence of a defect are discussed in Secs. III A and III B, respectively; the similar and different properties in the current-induced dynamics of FM and AFM skyrmions in a magnetic film with a defect, are given in Sec. IIIC. Finally, we conclude this work in Sec. IV.

II. METHODS

We consider a thin AFM film consisting of antiparallel magnetic moments $\boldsymbol{M}_1(\boldsymbol{r},t)$ and $\boldsymbol{M}_2(\boldsymbol{r},t)$ belonging to two magnetic sublattices with Dzyaloshinskii-Moriya (DM) interaction [42,43,52–54] identified to stabilize skyrmions. In particular, $|\boldsymbol{M}_1(\boldsymbol{r},t)| = |\boldsymbol{M}_2(\boldsymbol{r},t)| = M_s$, where M_s is the saturation magnetization, so that the total magnetization and AFM order parameter (i.e., the staggered magnetization) are defined as $\boldsymbol{M}(\boldsymbol{r},t) = \boldsymbol{M}_1(\boldsymbol{r},t) + \boldsymbol{M}_2(\boldsymbol{r},t)$ and $\boldsymbol{l}(\boldsymbol{r},t) = \boldsymbol{M}_1(\boldsymbol{r},t) - \boldsymbol{M}_2(\boldsymbol{r},t)$, respectively. In the following, we discuss the current-induced dynamics of an AFM skyrmion with $\boldsymbol{m}(\boldsymbol{r},t) = \boldsymbol{M}(\boldsymbol{r},t)/(2M_s)$ and the unit Néel vector $\boldsymbol{n}(\boldsymbol{r},t) = \boldsymbol{l}(\boldsymbol{r},t)/l = \boldsymbol{l}(\boldsymbol{r},t)/(2M_s)$.

Assuming that the easy-axis magnetic anisotropy is perpendicular to the xy plane and the DM interaction originates from the broken inversion symmetry at the interface, which is employed to stabilize the Néel-type skyrmion [30], the total AFM energy function then reads [28,30,55–60]

$$\varepsilon = \int \{\mu_0 H_{\rm ex} M_s \boldsymbol{m}^2 + A[(\nabla n_x)^2 + (\nabla n_y)^2 + (\nabla n_z)^2] - K n_z^2 + \omega_D\} dxdydz, \tag{1}$$

where $H_{\rm ex}$ and A are, respectively, the homogeneous and inhomogeneous exchange constants with $\mu_0 H_{ex}$ related to the lattice constant [61–63], and K is the PMA constant. Rewriting the micromagnetic energy limited to DMI in terms of $\boldsymbol{n}(\boldsymbol{r},t)$ and constant D leads to $\omega_D = D[n_z(\nabla\cdot\boldsymbol{n}) - (\boldsymbol{n}\cdot\nabla)n_z]$ [16,64–67]. According to the functional derivatives of the energy density, one can derive the effective fields $\boldsymbol{f}_{\boldsymbol{n}} = -\delta_{\boldsymbol{n}}\varepsilon/(\mu_0 M_s)$ and $\boldsymbol{f}_{\boldsymbol{m}} = -\delta_{\boldsymbol{m}}\varepsilon/(\mu_0 M_s)$. For $\boldsymbol{n}\times\boldsymbol{f}_{\boldsymbol{n}} = 0$, we can also find a static metastable AFM skyrmion solution characterized by the unit Néel vector $\boldsymbol{n} = (\sin\theta\cos\phi, \sin\theta\sin\phi, \cos\theta)$ in spherical coordinates [68]. Here, $\theta(\rho)$ only depends on ρ and $\phi = \varphi$ for Néel-type skyrmions, where (ρ,φ) are polar coordinates [28,30,67–70].

In the presence of spin currents, the equations of motion for both the magnetization $\boldsymbol{m}(\boldsymbol{r},t)$ and the unit Néel vector $\boldsymbol{n}(\boldsymbol{r},t)$ with the current-induced spin torque terms can be constructed as follow [56,57,59]:

$$\dot{\boldsymbol{n}} = \gamma \boldsymbol{f}_{\boldsymbol{m}}\times\boldsymbol{n} + \alpha_1 l\boldsymbol{n}\times\dot{\boldsymbol{m}} + \gamma H_D \boldsymbol{n}\times(\boldsymbol{m}\times\boldsymbol{p}), \tag{2a}$$

$$\dot{\boldsymbol{m}} = \gamma \boldsymbol{f}_{\boldsymbol{n}}\times\boldsymbol{n} + (\alpha_2/l)\boldsymbol{n}\times\dot{\boldsymbol{n}} + \gamma H_D \boldsymbol{n}\times(\boldsymbol{n}\times\boldsymbol{p}), \tag{2b}$$

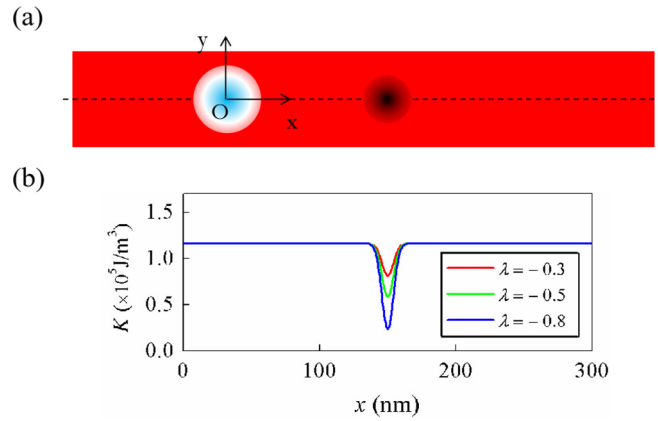

FIG. 1. The schematic illustration of an AFM racetrack with the considered defect. (a) Example of a defect located in front of an AFM skyrmion on a 300-nm-long racetrack, where the red area represents the AFM racetrack, the blue circle is skyrmion and the black spot denotes the defect. (b) The PMA constant K as a function of the position x for different defects, the size of which is fixed at $R_d = 6$ nm, along the dashed line in (a) where the spatial coordinate y is equal to 0.

where γ is the gyromagnetic ratio, α_1 and α_2 represent damping parameters, $H_D = \mu_B\theta_{\rm SH}J/(\gamma e M_s t_z)$ and $\boldsymbol{p}$ denote the effective field corresponding to damping-like spin torque and the unit electron polarization direction along y-axis ($\boldsymbol{p} = \boldsymbol{e}_y$) to drive the AFM skyrmion, respectively, $\theta_{\rm SH}$ is the effective spin-Hall angle with the default value of 0.1, μ_B is the Bohr magneton, e is the electron charge, J represents the driving current density and t_z is the film thickness.

To track the motion of the AFM skyrmion, we define the guiding center (R_x, R_y) of a skyrmion with [30,69,70]

$$R_u = \frac{\int u\boldsymbol{n}\cdot(\partial_x\boldsymbol{n}\times\partial_y\boldsymbol{n})dxdy}{\int \boldsymbol{n}\cdot(\partial_x\boldsymbol{n}\times\partial_y\boldsymbol{n})dxdy}, \quad u = x, y, \tag{3}$$

and then the AFM skyrmion velocity can be expressed as $(v_x, v_y) = (\dot{R}_x, \dot{R}_y)$. Therefore, one can numerically calculate the evolution of the unit Néel vector $\boldsymbol{n}(\boldsymbol{r},t)$ over time and determine the position and velocity of the AFM skyrmion at each moment according to Eqs. (2) and (3).

To study the interaction between the AFM skyrmion and defect caused by inhomogeneity, the defect is considered by the strength of PMA. We assume that the PMA changes locally and the value varies with position similar to Gaussian distribution in the defect region (see Fig. 1), meeting the following relation:

$$K = K_0[1.0 + \lambda e^{-\left(\frac{|\boldsymbol{r}-\boldsymbol{r}_d|}{R_d}\right)^2}], \tag{4}$$

where K_0 is the PMA constant in homogeneous area, $|\lambda|$ denotes the amplitude of variation referred as the strength of the defect, $\boldsymbol{r}_d$ is the position vector of defect center and R_d represents the characteristic size (i.e., the radius) of the defect. Such an anisotropy profile to represent the inhomogeneity induced by potential impurity sites, might be more realistic than a simple step-like defect or a defect with a linear variation of anisotropy, and is also analogous to the model proposed by

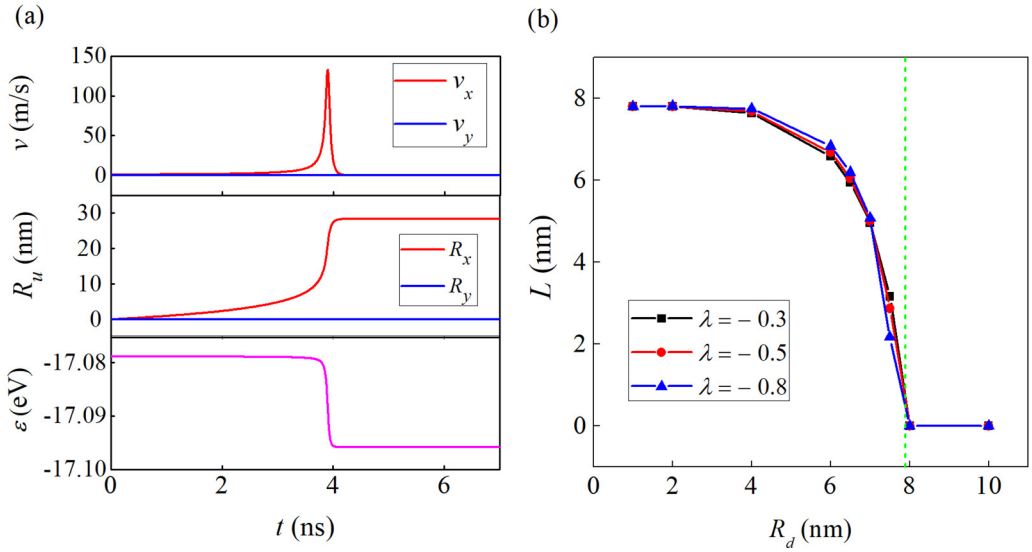

FIG. 2. The dynamic pinning process of an AFM skyrmion near the defect. (a) The skyrmion velocity, position and the total energy as a function of time when the initial distance L_0 between skyrmion and defect is 35 nm and the parameters of defect are: $\lambda = -0.5$ and $R_d = 6$ nm. (b) The distance L between the skyrmion final position and the defect center, as a function of the radius of defect for different strengths, where the green dashed line represents the radius of skyrmion.

Kronmüller [71]. Besides, similar profile of exchange interaction J_{ex} has also been used to discuss the skyrmion-defect interaction in FM film [44–45]. Our results for the interaction between the AFM skyrmion and defect are obtained based on this model, by numerically solving Eq. (2) with the method given in Ref. [72].

For numerical calculations, we consider the parameters of $KMnF_3$ samples [24,29,32,34]: saturation magnetization $Ms = 3.76 \times 10^5$ A/m, exchange stiffness $A = 6.59 \times 10^{-12}$ J/m and $\mu_0 H_{ex} = 39.89$ T, DMI constant is fixed at 8×10^{-4} J/m^2, PMA constant $K_0 = 1.16 \times 10^5$ J/m^3, and Gilbert damping coefficient $\alpha = \alpha_1 l = \alpha_2 / l = 0.1$. The default mesh size of $1.0 \times 1.0 \times 0.6\,\text{nm}^3$ is employed to discretize the AFM film, and all simulation is established at $T = 0$ K, ignoring the effect of thermal noise. In addition, both the defect and the AFM skyrmion are initially located on the centerline of a racetrack in all simulations, and the initial coordinate of skyrmion center is set as (0, 0).

III. RESULTS AND DISCUSSIONS

A. The process of dynamic pinning

First, a square AFM film with the size of $200 \times 200 \times 0.6\,\text{nm}^3$ is adopted. As the AFM skyrmion does not touch the film edge during its motion, the edge effect of the material is ignored. We consider a relaxed AFM skyrmion that is initially located at 35 nm away from the defect center and then begins to relax according to the AFM LLG Eq. (2) in the absence of any external driving forces. For the defect with $\lambda = -0.5$ and $R_d = 6.0$ nm, it can be seen from Fig. 2(a) that the AFM skyrmion gradually approaches the defect and eventually stops at 6.7 nm from its center, with the total energy changing from -17.079 eV to -17.096 eV. In this process, the velocity of skyrmion increases slowly first, and dramatically increases from 3.75 m/s at 3.0 ns to 135 m/s at 3.9 ns, and then rapidly decreases to 0 m/s at 4.5 ns. To get a more general conclusion, we also systematically investigate the effect of defect with different size and strength on the pinning process of an AFM skyrmion. Especially, there is a detailed description for the case of $\lambda < 0$. Figure 2(b) describes the distance L between final relaxed position of the skyrmion and the center of the defect versus the defect parameters. It can be seen that the AFM skyrmion final position is not sensitive to the strength of the defect, but mainly depends on its size. More specifically, when the radius R_d of defect is smaller than the AFM skyrmion radius R_s (which is defined as the distance between $n_z = -1$ and $n_z = 0$, and extracted from Ref. [68]) with the default value in our calculations being about 7.9 nm, the skyrmion stops at the off-center of the defect, and L gradually decreases as R_d increases. When R_d is close to R_s, L drops sharply and approaches 0, and if R_d exceeds R_s, then the skyrmion will stay at the center of the defect ($L = 0$). Also, the dynamic behavior of the AFM skyrmion is analogous to that of the FM skyrmion in Ref. [47], where the preferred pinning position of skyrmion depends strongly on the ratio of skyrmion size to the defect size, justifying the reliability of our results. It also should be mentioned that the pinning effect may be reduced or suppressed due to the thermal agitation in experiments at finite temperatures, which depends on the parameters (including the size and strength) of defects and thermal noise.

In addition, when the initial position of the AFM skyrmion is far from the defect, the interaction between the defect and skyrmion is almost negligible. However, when skyrmion is placed in the area (in the range of approximately 100 nm away from the defect center in this work) where the defect can interact with it, the AFM skyrmion will start to move and eventually be pinned at the same position for the same defect, which is independent of the initial distance L_0. This interesting phenomenon will be analyzed in detail from the perspective of energy when discussing the depinning process of an AFM skyrmion in the next section.

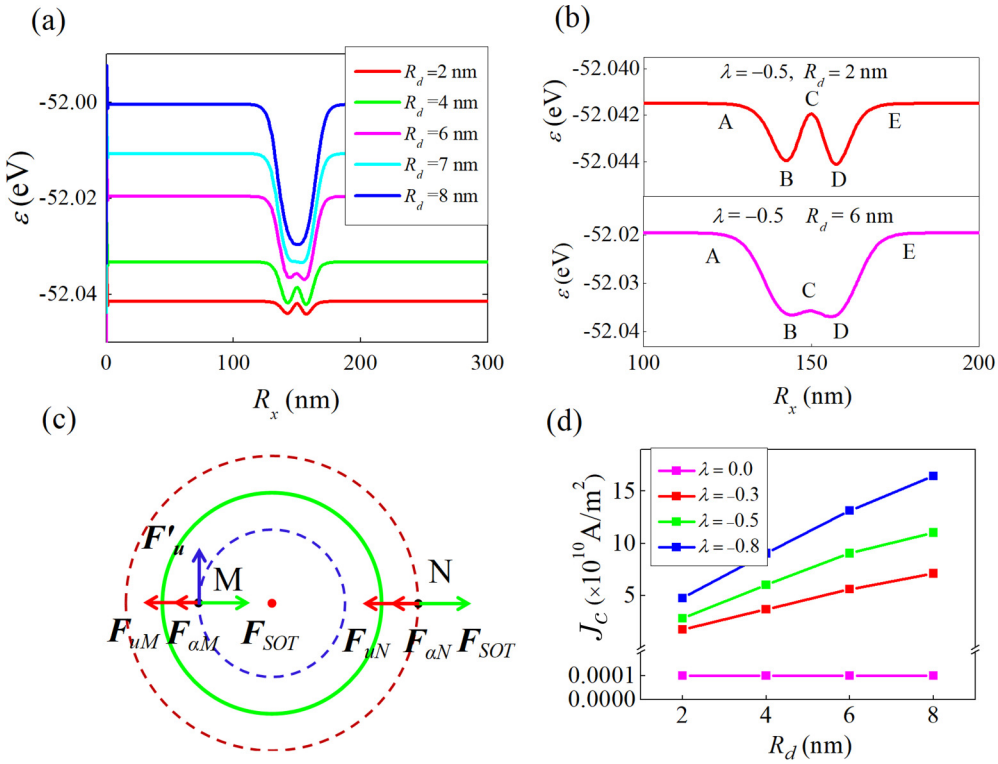

FIG. 3. (a) The variation of the total energy with the skyrmion position R_x is plotted for different defect sizes. Here, the driving current density is fixed at 11.2 $\times 10^{10}$ A/m^2, $L_0 = 150$ nm and $\lambda = -0.5$. (b) The enlarged view of the cases where $R_d = 2$ nm and $R_d = 6$ nm in (a), the letters A, B, C, D, E represent five different specific positions. (c) The schematic diagram of the force exerted on the AFM skyrmion at different positions. (d) The critical current density required to force the skyrmion to pass through defect successfully, as a function of defect size for different strength λ.

B. The process of dynamic depinning

We further explore the effect of a defect on the AFM skyrmion motion in the racetrack. Here, the spin current is considered as the driving force, and an AFM skyrmion encounters defect during the motion as shown in Fig. 1(a), where the defect is located at 150 nm in front of the skyrmion. To acquire a stable velocity and an accurate study of the motion behavior of AFM skyrmion, the sample size of 200 × 600 × 0.6 nm^3 is adopted for the dynamic depinning process. When the current density is small, the driving force provided by the spin current is insufficient for the AFM skyrmion to overcome the energy barrier of the defect, so that the skyrmion is pinned and finally stops at the off-center of the defect. However, for a large current density, the skyrmion can pass through the defect area successfully, and its speed merely changes in the defect area.

To understand the physics behind the dynamic behavior of the AFM skyrmion mentioned above, Fig. 3(a) shows the relation between the total energy of the system and the AFM skyrmion position R_x for different sizes of defect with $\lambda < 0$ when the skyrmion can pass the inhomogeneous region. Obviously, when $R_d < R_s$, the energy curve has two local minimal values near the defect center, while for $R_d > R_s$, it has only one minimal value at the center of defect. Moreover, without any external driving forces, the AFM skyrmion prefers to be in the low-energy place which is related to the trough in the energy curve. Therefore, one can understand that the skyrmion is pinned at the center of defect for $R_d > R_s$, off-center of defect for $R_d < R_s$, and stops at the same position for the same defect, which are mentioned in Sec. IIIA. Besides, for the defects with same size and different strength (when $\lambda < 0$), the corresponding energy curves have the same shapes. Let us review the pinning process of the AFM skyrmion again, one can also understand why the skyrmion final position is not sensitive to the strength of the defect, but mainly depends on its size.

Considering the current-induced skyrmion motion for $\lambda < 0$, when $R_d > R_s$, the AFM skyrmion is pinned to the right end of the defect for a small driving current density and passes through the defect region successfully for a large one. Also, the AFM skyrmion is moving along a straight line in the both situations. However, when $R_d < R_s$, there may be four motion behaviors of the AFM skyrmion for the different parameters of driving current density and defect. We now analyze the complex phenomenon from the perspective of energy and force. For ease of understanding, the force $\boldsymbol{F_u}$ arising from the defect is obtained by $\boldsymbol{F_u} = -\nabla\varepsilon$, where $\varepsilon(R_x, R_y)$ is the total potential energy of the given system, and (R_x, R_y) is the position vector of the skyrmion center. Besides, there is also a dissipative force F_α being equivalent to the frictional force in classical motion of a massive particle due to the finite Gilbert damping, and an external force F_{SOT} arising from the damping-like component of spin-orbit torque (SOT) [56]. A schematic diagram is also presented [see Fig. 3(c)], where the

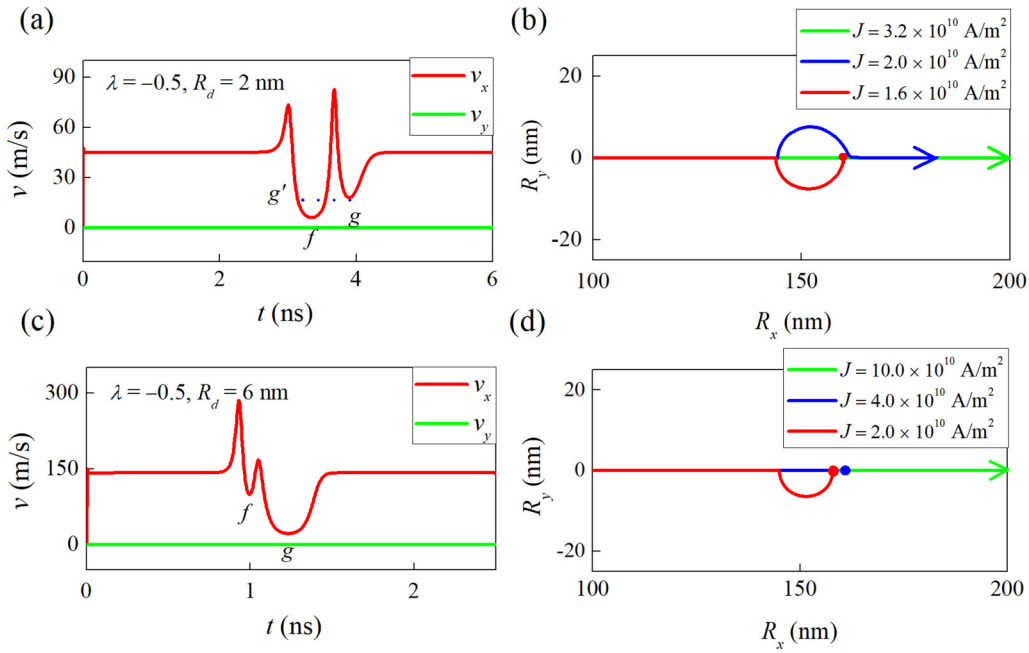

FIG. 4. The velocity v and trajectory of an AFM skyrmion driven by the spin current in different conditions. (a) $J = 3.2 \times 10^{10}$ A/m^2, (b) $\lambda = -0.5$ and $R_d = 2$ nm, (c) $J = 10.0 \times 10^{10}$ A/m^2, (d) $\lambda = -0.5$ and $R_d = 6$ nm. Here, the arrow indicates that AFM skyrmion will go forward in the direction of its, and the filled circle means the skyrmion will be trapped.

green line corresponds to the points B and D in Fig. 3(b), and the red dot is the defect center, i.e., point C in Fig. 3(b). From Fig. 3(b), we can see that the energy curves corresponding to both the small (taking $R_d = 2.0$ nm as an example) and the large (taking $R_d = 6.0$ nm as an example) defects have two minimal values and one maximal value. But their amplitudes of variation are different, which will cause a significant difference in the motion of skyrmion.

First, for the case of $R_d = 2.0$ nm, it is found that the maximum of the force $\boldsymbol{F_u}$ (i.e., $\boldsymbol{F_{u1}}$) between the points B and C is larger than that (i.e., $\boldsymbol{F_{u2}}$) between the points D and E. Meanwhile, if the skyrmion can pass the defect, then the minimum velocity between the points B and C is smaller than that between the points D and E as shown in Fig. 4(a), i.e., $v_f < v_g$. Therefore, the AFM skyrmion has three motion behaviors in this situation. Assuming the driving current density is not large enough, when the skyrmion moves to the point M in Fig. 3(c), the driving force $\boldsymbol{F}_{\rm SOT}$, dissipative force $\boldsymbol{F}_{\alpha M}$ and the repulsive force $\boldsymbol{F}_{uM}$ arising from the defect are completely offset in the horizontal direction. But in the vertical direction, if the skyrmion is going up or down, then the total energy of the system will decrease, so that the additional force $\boldsymbol{F'}_u$ caused by the energy gradient is created and the skyrmion may start moving to the place where the energy is low. Because the green circle represents the minimum of energy, the skyrmion cannot be infinitely far away from the defect but is confined to the vicinity of the green line and moves to the right end of the defect. If the driving current density is small ($F_{\rm SOT} = F_{uM} + F_{\alpha M}$, and $F_{\rm SOT} < F_{u2} + F_{\alpha 2}$), then the force in the horizontal direction reaches equilibrium once again when the skyrmion circles the defect from the point M to the point N in Fig. 3(c) [corresponding to a certain position between points D and E in Fig. 3(b)]. But in the vertical direction, whether the skyrmion is up or down, the energy will increase, so there is no additional force $\boldsymbol{F'}_u$, and the skyrmion is finally trapped at the point N. However, if the current is slightly larger ($F_{\rm SOT} = F_{uM} + F_{\alpha M}$, and $F_{u2} + F_{\alpha 2} < F_{\rm SOT} < F_{u1} + F_{\alpha 1}$), the skyrmion will still surround from the left side of the defect to the right side of it, the skyrmion will get rid of the constraint of the right end of the defect and successfully pass through the defect area, although it may slightly deviate from its original orbit. Furthermore, if the driving current density is large enough, then $F_{\rm SOT}$ is always greater than $F_u + F_\alpha$, thus the skyrmion will smoothly pass the defect area along a straight line shown in Fig. 4(b). In this case, the dependence of the skyrmion motion behaviors and the driving current density is similar to that in Ref. [50], where the defect is modeled by a vacancy in FM film.

On the other hand, when $R_d = 6.0$ nm, we can obtain $F_{u1} < F_{u2}$ and $v_f > v_g$ [see Fig. 4(c)]. For this situation, there are also three motion behaviors of the AFM skyrmion, which are slightly different from the case of $R_d = 2.0$ nm. First, for the small driving current density, the AFM skyrmion moves to the point M in Fig. 3(c), the driving force $\boldsymbol{F}_{\rm SOT}$, dissipative force $\boldsymbol{F}_{\alpha M}$ and the repulsive force $\boldsymbol{F}_{uM}$ are completely offset in the horizontal direction. At this time, $F_{\rm SOT} = F_{uM} + F_{\alpha M}$, and $F_{\rm SOT} < F_{u1} + F_{\alpha 1}$, similar to the case of $R_d = 2.0$ nm, the skyrmion will surround the defect to its right end and be trapped at point N [see Fig. 3(c)]. Second, if the driving current density is slightly larger ($F_{u1} + F_{\alpha 1} < F_{\rm SOT} < F_{u2} + F_{\alpha 2}$), then the skyrmion moves along a straight line to a certain point between the points D and E and then is pinned. Finally, if the driving current density is large enough, then the equation $F_{\rm SOT} > F_u + F_\alpha$ is always satisfied, thus, the AFM skyrmion successfully passes through the defect area along the driving current [see Fig. 4(d)].

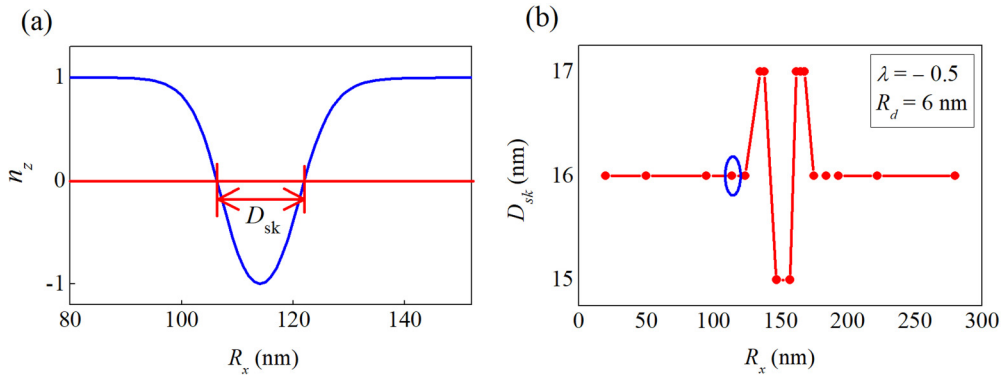

FIG. 5. (a) The skyrmion diameter is defined as the diameter of the circle where $n_z = 0$. (b) The skyrmion diameter as a function of the position. Here, the skyrmion profile in (a) corresponds to the point in the blue circle of (b).

According to the discussion above, it is found that, in any case, there will always be a critical current density J_c, which makes the AFM skyrmion pass through the defect area successfully along a straight line we expected. In particular, Fig. 3(d) illustrates that the critical current density versus the size and strength of the defect. It can be seen that for the same intensity of defect, the critical driving current density is proportional to the value of R_d, and for the same radius of defect, the pinning effect is enhanced with increasing strength of the defect. It is worth mentioning that the magnitude of the critical current density J_c is not only related to the radius of defect, but also depends on its strength. Moreover, compared with the homogeneous racetrack where $\lambda = 0$ ($\sim 10^6$ A/m^2), the critical depinning current density J_c ($\sim 10^{10}$ A/m^2) required to displace the skyrmion in a defective racetrack obviously increases, which implies that the effect of defect is vital in the future spintronic devices-based AFM skyrmions.

In addition, the variation of skyrmion size occurs in the depinning process as shown in Fig. 5. The skyrmion diameter is constant in homogeneous area, $D_{sk} = 16$ nm. As the skyrmion approaches to the center of the defect, its size will increase to 17 nm since the value of anisotropy is getting smaller, similar to the case where the reduced anisotropy can increase the domain wall width. Also, if the centers of the skyrmion and defect are almost coincident, then the size will shrink again ($D_{sk} = 15$ nm). The reason is that the surrounding K is higher than that of the defect center, which results in the compression of the skyrmion. Although the size of skyrmion changes between 17 and 15 nm, the variation is not obvious and the topological structure and stability are maintained, we still treat the skyrmion as a rigid object.

A similar depinning process is found for $\lambda > 0$. Under different driving currents density, the AFM skyrmion may be pinned or keep moving in the defect area. Here, the situation, where the skyrmion is pinned to the right end of the defect after it made a detour, will disappear. Considering of the case $\lambda > 0$, when skyrmion is in the defect region, the total energy of the system is always higher than that when the skyrmion in the homogeneous region. Therefore, if the driving force provided is insufficient, then there is no restriction of green circle that appears in case of $\lambda < 0$ [see Fig. 3(c)] on the skyrmion, so that it can gradually deviate from the defect until the effect of the defect on it is very weak. Finally, the skyrmion can continue to move along the current direction [68]. Generally, the impurities may cause changes in other material properties, such as Heisenberg exchange constant and DMI constant. We also model the defect with the strength of A and D and the results are shown in Ref. [68].

C. Comparison of the effect of defect on FM and AFM skyrmions

In the following, we make a comparison between the motion of a FM skyrmion and an AFM skyrmion in the presence of a defect. Taking the spin current into account [68], the FM skyrmion has both the longitudinal and transverse velocities, which are parallel and perpendicular to the direction of injected current, respectively [5,16–18]. The latter, caused by the nonzero Magnus force ($4\pi Q \times v$) due to the skyrmion number Q ($= +1$ or -1) [2,5,18,68–70], leads to the deviation of the skyrmion from the driving current direction. Such a phenomenon is called as the skyrmion Hall effect [73–76]. However, in the AFM system, which has two magnetic sublattices coupled by a strong inter-sublattice exchange field, the adjacent magnetic moments are in opposite directions [38,77]. As a result, the AFM skyrmion can be regarded as a combination of two FM skyrmions with opposite magnetic moment distributions. Therefore, the AFM skyrmion will move along the driving current direction without showing the skyrmion Hall effect, since the opposite skyrmion topological numbers ($Q = \pm 1$) belonging to the two sublattices results in a prefect compensation of sublattice Magnus forces [23,24,30]. Our findings reveal that these differences not only influence the velocity of skyrmions, but also affect the skyrmion-defect interaction as shown in the following paragraph.

When $\lambda < 0$, the AFM skyrmion will either be captured at the defect area or make a detour when the driving current is smaller than the critical current density J_c required to displace skyrmion from defect, and pass through the defect to the other end of the racetrack for larger current density ($J > J_c$) keeping the direction of motion unchanged, as described previously. For the FM skyrmion [44–45,47], the behavior is analogous to that of the AFM skyrmion, nevertheless, the difference is that the FM skyrmion will rotate around the defect and stop gradually due to the Magnus force for small current density [68]. However, for $\lambda > 0$, there is a significant difference between

the FM and AFM skyrmions. The FM skyrmion can always bypass the defect, and finally move forward in the original direction, while the AFM skyrmion has three situations which are pinned, making a detour and going straight [68]. Considering the applications based on skyrmions, such as the racetrack memory, the pinning of skyrmions will seriously influence the transmission of information. Therefore, the study of the effect of defect on skyrmion is particularly important. Meanwhile, when $\lambda > 0$, the AFM skyrmion might still be trapped, unlike FM skyrmion which can always bypass the defect. It means that the defect with $\lambda > 0$ has a greater influence on the motion behaviors of AFM skyrmions than on that of FM skyrmions.

IV. CONCLUSIONS

In conclusion, we have systematically investigated the interaction between a single AFM skyrmion and a defect with different parameters, and we discussed the effect of the defect on the current-induced motion of the AFM skyrmion. The results show that, generally, the AFM skyrmion will be repelled by the defect with $\lambda > 0$ and attracted by that arising from spatial decrease in PMA (that is $\lambda < 0$). However, both types of defects act as pinning sites, which can result in an effective slowdown or even capturing of the AFM skyrmion during its motion. We also studied the transition from the pinned to the depinned state of an AFM skyrmion when it moves on a racetrack with a defect. It is found that the critical depinning current density increases with increasing defect strength and is proportional to the radius of the defect. Furthermore, we provided a reasonable explanation from the viewpoint of energy landscape for typical behaviors of the AFM skyrmion. Finally, the dynamic pinning and depinning processes of AFM skyrmion have been compared against the FM skyrmion, which reveals that the FM skyrmion can easily bypass the defect when $\lambda > 0$, while the AFM skyrmion may still be trapped, where the difference between the both could be attributed to the Magnus force. Our findings can provide a reliable guidance for future design of next-generation spintronic devices-based AFM skyrmions, because the magnitude of the driving current density required in actual operation could be estimated on the basis of our results. However, it should be noted that the results are reasonable for experiments and applications at low temperatures, where thermal agitation is not strong.

ACKNOWLEDGMENTS

G.Z. acknowledges the support by the National Natural Science Foundation of China (Grants No. 51771127, No. 51571126, and No. 51772004) of China, the Scientific Research Fund of Sichuan Provincial Education Department (Grants No. 18TD0010 and No. 16CZ0006). X.Z. was supported by the Presidential Postdoctoral Fellowship of the Chinese University of Hong Kong, Shenzhen (CUHKSZ). Y.Z. acknowledges the support by the President's Fund of CUHKSZ, Longgang Key Laboratory of Applied Spintronics, National Natural Science Foundation of China (Grants No. 11974298 and No. 61961136006), Shenzhen Fundamental Research Fund (Grant No. JCYJ20170410171958839), and Shenzhen Peacock Group Plan (Grant No. KQTD20180413181702403).

[1] U. K. Rößler, A. N. Bogdanov, and C. Pfleiderer, Nature (London) **442**, 797 (2006).
[2] N. Nagaosa and Y. Tokura, Nat. Nanotechnol. **8**, 899 (2013).
[3] G. Finocchio, F. Büttner, R. Tomasello, M. Carpentieri, and M. Kläui, J. Phys. D: Appl. Phys. **49**, 423001 (2016).
[4] W. Kang, Y. Huang, X. Zhang, Y. Zhou, and W. Zhao, Proc. IEEE **104**, 2040 (2016).
[5] A. Fert, N. Reyren, and V. Cros, Nat. Rev. Mat. **2**, 17031 (2017).
[6] X. Zhang, M. Ezawa, and Y. Zhou, Sci. Rep. **5**, 9400 (2015).
[7] T. Nozaki, Y. Jibiki, M. Goto, E. Tamura, T. Nozaki, H. Kubota, A. Fukushima, S. Yuasa, and Y. Suzuki, Appl. Phys. Lett. **114**, 012402 (2019).
[8] Y. Zhou, Natl Sci. Rev. **6**, 210 (2019).
[9] S. Mühlbauer, B. Binz, F. Jonietz, C. Pfleiderer, A. Rosch, A. Neubauer, R. Georgii, and P. Böni, Science **323**, 915 (2009).
[10] A. Neubauer, C. Pfleiderer, B. Binz, A. Rosch, R. Ritz, P. G. Niklowitz, and P. Böni, Phys. Rev. Lett. **102**, 186602 (2009).
[11] F. Jonietz, S. Mühlbauer, C. Pfleiderer, A. Neubauer, W. Münzer, A. Bauer, T. Adams, R. Georgii, P. Böni, R. A. Duine, K. Everschor, M. Garst, and A. Rosch, Science **330**, 1648 (2010).
[12] W. Münzer, A. Neubauer, T. Adams, S. Mühlbauer, C. Franz, F. Jonietz, R. Georgii, P. Böni, B. Pedersen, M. Schmidt, A. Rosch, and C. Pfleiderer, Phys. Rev. B **81**, 041203(R) (2010).
[13] X. Z. Yu, Y. Onose, N. Kanazawa, J. H. Park, J. H. Han, Y. Matsui, N. Nagaosa, and Y. Tokura, Nature **465**, 901 (2010).
[14] X. Z. Yu, N. Kanazawa, Y. Onose, K. Kimoto, W. Z. Zhang, S. Ishiwata, Y. Matsui, and Y. Tokura, Nat. Mater. **10**, 106 (2011).
[15] K. Shibata, X. Z. Yu, T. Hara, D. Morikawa, N. Kanazawa, K. Kimoto, S. Ishiwata, Y. Matsui, and Y. Tokura, Nat. Nanotechnol. **8**, 723 (2013).
[16] J. Sampaio, V. Cros, S. Rohart, A. Thiaville, and A. Fert, Nat. Nanotechnol. **8**, 839 (2013).
[17] J. Iwasaki, M. Mochizuki, and N. Nagaosa, Nat. Nanotechnol. **8**, 742 (2013).
[18] X. Zhang, G. P. Zhao, H. Fangohr, J. P. Liu, W. X. Xia, J. Xia, and F. J. Morvan, Sci. Rep. **5**, 7643 (2015).
[19] R. E. Troncoso and A. S. Núñez, Phys. Rev. B **89**, 224403 (2014).
[20] R. Wiesendanger, Nat. Rev. Mater. **1**, 16044 (2016).
[21] S. Woo, K. Litzius, B. Krüger, M. Y. Im, L. Caretta, K. Richter, M. Mann, A. Krone, R. M. Reeve, M. Weigand, P. Agrawal, I. Lemesh, M.-A. Mawass, P. Fischer, M. Klaui, and G. S. D. Beach, Nat. Mater. **15**, 501 (2016).
[22] S. S. Parkin, M. Hayashi, and L. Thomas, Science **320**, 190 (2008).
[23] X. Zhang, Y. Zhou, and M. Ezawa, Sci. Rep. **6**, 24795 (2016).
[24] J. Barker and O. A. Tretiakov, Phys. Rev. Lett. **116**, 147203 (2016).

[25] P. Bessarab, D. Yudin, D. Gulevich, P. Wadley, M. Titov, and O. A. Tretiakov, Phys. Rev. B **99**, 140411(R) (2019).
[26] Z. Liu and H. Ian, Chem. Phys. Lett. **649**, 135 (2016).
[27] P. M. Buhl, F. Freimuth, S. Blügel, and Y. Mokrousov, Phys. Status Solidi RRL **11**, 1700007 (2017).
[28] H. Velkov, O. Gomonay, M. Beens, G. Schwiete, A. Brataas, J. Sinova, and R. A. Duine, New J. Phys. **18**, 075016 (2016).
[29] H. Xia, C. Jin, C. Song, J. Wang, J. Wang, and Q. Liu, J. Phys. D **50**, 505005 (2017).
[30] L. Shen, J. Xia, G. Zhao, X. Zhang, M. Ezawa, O. A. Tretiakov, X. Liu, and Y. Zhou, Phys. Rev. B **98**, 134448 (2018).
[31] V. Baltz, A. Manchon, M. Tsoi, T. Moriyama, T. Ono, and Y. Tserkovnyak, Rev. Mod. Phys. **90**, 015005 (2018).
[32] C. Jin, C. Song, J. Wang, and Q. Liu, Appl. Phys. Lett. **109**, 182404 (2016).
[33] B. Göbel, A. Mook, J. Henk, and I. Mertig, Phys. Rev. B. **96**, 060406(R) (2017).
[34] X. Zhao, R. Ren, G. Xie, and Y. Liu, Appl. Phys. Lett. **112**, 252402 (2018).
[35] H. Yang, C. Wang, T. Yu, Y. Cao, and P. Yan, Phys. Rev. Lett. **121**, 197201 (2018).
[36] H. Yang, C. Wang, X. Wang, X. S. Wang, Y. Cao, and P. Yan, Phys. Rev. B **98**, 014433 (2018).
[37] A. H. MacDonald and M. Tsoi, Philos. Trans. Roy. Soc. London A: Math. Phys. Eng. Sci. **369**, 3098 (2011).
[38] O. Gomonay, V. Baltz, A. Brataas, and Y. Tserkovnyak, Nat. Phys. **14**, 213 (2018).
[39] T. Jungwirth, X. Marti, P. Wadley, and J. Wunderlich, Nat. Nanotechnol. **11**, 231 (2016).
[40] R. Lebrun, A. Ross, S. A. Bender, A. Qaiumzadeh, L. Baldrati, J. Cramer, A. Brataas, R. A. Duine, and M. Kläui, Nature **561**, 222 (2018).
[41] M. B. Jungfleisch, W. Zhang, and A. Hoffmann, Phys. Lett. A **382**, 865 (2018).
[42] I. Dzyaloshinsky, J. Phys. Chem. Solids **4**, 241 (1958).
[43] T. Moriya, Phys. Rev. **120**, 91 (1960).
[44] S.-Z. Lin, C. Reichhardt, C. D. Batista, and A. Saxena, Phys. Rev. B **87**, 214419 (2013).
[45] Y.-H. Liu and Y.-Q. Li, J. Phys.: Condens. Matter **25**, 076005 (2013).
[46] J. V. Kim and M. W. Yoo, Appl. Phys. Lett. **110**, 132404 (2017).
[47] D. Stosic, T. B. Ludermir, and M. V. Milošević, Phys. Rev. B **96**, 214403 (2017).
[48] I. Lima Fernandes, J. Bouaziz, S. Blügel, and S. Lounis, Nat. Commun. **9**, 4395 (2018).
[49] C. Hanneken, K. Kubetzka, A. von Bergmann, and R. Wiesendanger, New J. Phys. **18**, 055009 (2016).
[50] J. Müller and A. Rosch, Phys. Rev. B **91**, 054410 (2015).
[51] R. L. Silva, R. C. Silva, A. R. Pereira, and W. A. Moura-Melo, J. Phys. Condens Matter. **31**, 225802 (2019).
[52] I. E. Dzyaloshinskii, Sov. Phys. JETP **19**, 960 (1964).
[53] T. Moriya, Phys. Rev. Lett. **4**, 228 (1960).
[54] H. Yang, A. Thiaville, S. Rohart, A. Fert, and M. Chshiev, Phys. Rev. Lett. **115**, 267210 (2015).
[55] A. N. Bogdanov, U. K. Rößler, M. Wolf, and K. H. Müller, Phys. Rev. B **66**, 214410 (2002).
[56] E. G. Tveten, A. Qaiumzadeh, O. A. Tretiakov, and A. Brataas, Phys. Rev. Lett. **110**, 127208 (2013).
[57] T. Shiino, S. H. Oh, P. M. Haney, S. W. Lee, G. Go, B. G. Park, and K. J. Lee, Phys. Rev. Lett. **117**, 087203 (2016).
[58] E. M. Lifshitz and L. P. Pitaevskii, *Statistical Physics, Course of Theoretical Physics* (Pergamon, Oxford, 1980), Vol. 9.
[59] K. M. D. Hals, Y. Tserkovnyak, and A. Brataas, Phys. Rev. Lett. **106**, 107206 (2011).
[60] S. A. Bender, H. Skarsvåg, A. Brataas, and R. A. Duine, Phys. Rev. Lett. **119**, 056804 (2017).
[61] V. G. Bar'yakhtar, B. A. Ivanov, and M. V. Chetkin, Sov. Phys. Usp. **28**, 563 (1985).
[62] N. Papanicolaou, Phys. Rev. B **51**, 15062 (1995).
[63] E. G. Tveten, T. Müller, J. Linder, and A. Brataas, Phys. Rev. B **93**, 104408 (2016).
[64] A. Fert, V. Cros, and J. Sampaio, Nat. Nanotechol. **8**, 152 (2013).
[65] A. Thiaville, S. Rohart, E. Jué, V. Cros, and A. Fert, Europhys. Lett. **100**, 57002 (2012).
[66] A. N. Bogdanov and U. K. Rößler, Phys. Rev. Lett. **87**, 037203 (2001).
[67] S. Rohart and A. Thiaville, Phys. Rev. B **88**, 184422 (2013).
[68] See Supplemental Material at http://link.aps.org/supplemental/10.1103/PhysRevB.100.144439 for details on the static metastable AFM skyrmion solution, the dynamic depinning process of an AFM skyrmion when $\lambda > 0$, the effect of exchange constant and DMI constant on AFM skyrmion, and the dynamics of a FM skyrmion in the presence of a defect.
[69] S. Komineas and N. Papanicolaou, Phys. Rev. B **92**, 174405 (2015).
[70] S. Komineas and N. Papanicolaou, Phys. Rev. B **92**, 064412 (2015).
[71] H. Kronmüller, Physica Status Solidi B **144**, 385 (1987).
[72] C. Serpico, I. D. Mayergoyz, and G. Bertotti, J. Appl. Phys. **89**, 6991 (2001).
[73] X. Zhang, Y. Zhou, and M. Ezawa, Nat. Commun. **7**, 10293 (2016).
[74] P. Lai, G. P. Zhao, H. Tang, N. Ran, S. Q. Wu, J. Xia, X. Zhang, and Y. Zhou, Sci. Rep. **7**, 45330 (2017).
[75] W. Jiang, X. Zhang, G. Yu, W Zhang, X. Wang, M. B. Jungfleisch, J. E. Pearson, X. Cheng, O. Heinonen, K. L.Wang, Y. Zhou, A. Hoffmann, and S. G. E. Velthuis, Nat. Phys. **13**, 162 (2017).
[76] S. Woo, K. M. Song, X. Zhang, Y. Zhou, M. Ezawa, X. Liu, S. Finizio, J. Raabe, N. J. Lee, S. I. Kim, S. Y. Park, Y. Kim, J. Y. Kim, D. Lee, O. Lee, J. W. Choi, B. C. Min, H. C. Koo, and J. Chang, Nat. Commun. **9**, 959 (2018).
[77] F. Keffer and C. Kittel, Phys. Rev. **85**, 329 (1952).